

# Efficient Real-World Autonomous Racing via Attenuated Residual Policy Optimization

Raphael Trumpp, Denis Hoornaert, Mirco Theile, and Marco Caccamo  
Technical University of Munich  
Munich, Germany  
Email: {raphael.trumpp, denis.hoornaert, mirco.theile, mcaccamo}@tum.de

**Abstract**—Residual policy learning (RPL), in which a learned policy refines a static base policy using deep reinforcement learning (DRL), has shown strong performance across various robotic applications. Its effectiveness is particularly evident in autonomous racing, a domain that serves as a challenging benchmark for real-world DRL. However, deploying RPL-based controllers introduces system complexity and increases inference latency. We address this by introducing an extension of RPL named attenuated residual policy optimization ( $\alpha$ -RPO). Unlike standard RPL,  $\alpha$ -RPO yields a standalone neural policy by progressively attenuating the base policy, which initially serves to bootstrap learning. Furthermore, this mechanism enables a form of privileged learning, where the base policy is permitted to use sensor modalities not required for final deployment. We design  $\alpha$ -RPO to integrate seamlessly with PPO, ensuring that the attenuated influence of the base controller is dynamically compensated during policy optimization. We evaluate  $\alpha$ -RPO by building a framework for 1:10-scaled autonomous racing around it. In both simulation and zero-shot real-world transfer to Roboracer cars,  $\alpha$ -RPO not only reduces system complexity but also improves driving performance compared to baselines—demonstrating its practicality for robotic deployment. Our code is available at: [https://github.com/raphajaner/arp0\\_racing](https://github.com/raphajaner/arp0_racing).

## I. INTRODUCTION

Once primarily confined to arcade games [15], deep reinforcement learning (DRL) is now being successfully employed across a wide range of real-world domains [23]. However, deployment in real-world autonomous systems introduces new practical challenges, notably in the form of the widely discussed sim-to-real gap and the corresponding complicated task of thorough testing. Prior research has attempted to facilitate learning for such autonomous applications by introducing residual policy learning (RPL) [21, 13]. In this training paradigm, a DRL policy is trained to refine the output of a fixed base policy, typically a classical controller, which serves as a strong inductive bias during learning. RPL has been successfully applied to robotic applications such as manipulation [21, 13, 12], legged locomotion [14], drone control [31], and particularly autonomous racing [6, 30, 25, 26].

As an application, the 1:10-scaled autonomous racing series called Roboracer [17, 7], formerly known as F1TENTH, has emerged as a prime testbed for learning-based methods as it demands both real-time decision-making and robustness to uncertain conditions while providing well-defined objectives. Moreover, the ecosystem comes with a broad collection of controllers to compare or use as a base policy for RPL. As such, a large set of classical racing methods typically

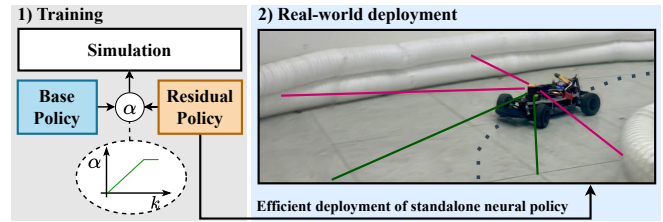


Fig. 1: We test our proposed  $\alpha$ -RPO method by learning competitive real-world racing behavior with 1:10-scaled autonomous Roboracer cars. Compared to classical RPL,  $\alpha$ -RPO attenuates the contribution of the base policy during training, improving final performance while yielding a standalone neural policy at inference time for efficient deployment.

relies on offline racing line optimization and subsequent path tracking for deployment [3]. Although successful in Roboracer events [2], this approach is not fully autonomous; it depends on pre-computed global trajectories, rendering it unable to adapt to new environments online. Thus, reactive mapless methods, such as the follow-the-gap (FTG) controller [20], remain a popular choice for their reliability in real-world Roboracer competitions.

Recent work demonstrated the effectiveness of RPL for autonomous racing in the classical offline case [25, 11, 10] and in the reactive online scenario [30, 26]; they also include successful real-world deployments [10, 11]. A remaining primary challenge when using RPL is deciding on the static mixing parameter between the base and residual policies. Giving more weight to the residual policy might destabilize early training through poor random decisions. However, later in training, it may be necessary to allow the agent to override the base policy’s decisions. Popular methods [11, 25] simply restrict the scale of the residual policy’s total contribution to stabilize early training, meaning these works cannot fully explore the agent’s potential. In addition, these RPL-based agents must execute the base policy during deployment, thereby inheriting its specific input modality requirements. This dependence is particularly prohibitive when the base policy relies on localization, as it increases computation and complicates real-world deployment.

Currently, the prevailing approach in RPL relies on summing the base and residual actions with a static mixing factor. Only a few studies have explored adaptive aggregation techniques, e.g., [1, 12] present aggregation techniques for

multiple base policies. Similarly, Nakhaei et al. [16] employ an adaptive mixing to bridge the gap between offline and online settings. However, their method primarily modulates the base policy to mitigate dynamics shifts without removing it. The full attenuation during online RPL training has not yet been a targeted objective, despite the compelling motivation for it.

Accordingly, we introduce attenuated residual policy optimization ( $\alpha$ -RPO), in which the weight of the base policy is gradually *attenuated to zero* throughout training. Thus,  $\alpha$ -RPO takes advantage of the early strong inductive bias of the base policy to bootstrap learning while allowing the residual policy to make categorically different decisions at the end of training. However, an implication of continuously altering the weighing between the base and residual policies is that the environment is non-stationary from the perspective of the residual policy during training. We mitigate this aspect by integrating  $\alpha$ -RPO directly into proximal policy optimization (PPO) [19], employing PPO’s importance sampling-based objective to compensate for the non-stationarity induced by the weight attenuation schedule.

Since  $\alpha$ -RPO yields a standalone neural policy at the end of training, real-world deployment is significantly simplified alongside possible fast GPU-based inference. This inference efficiency mirrors that of lightweight behavior cloning (BC) architectures like TinyLidarNet [29], but  $\alpha$ -RPO optimizes the policy via active interaction to ensure robustness to unseen states and the ability to outperform the base policy. Moreover,  $\alpha$ -RPO naturally avoids the common catastrophic forgetting inherent to teacher-student approaches such as [28], thereby improving stability. Additionally,  $\alpha$ -RPO stands in contrast to methods such as FastRLAP [22], which are designed specifically for real-world fine-tuning of a base policy; our method instead is designed for zero-shot real-world transfer of a standalone neural policy after training in simulation.

Given the Roboracer platform’s suitability as a real-world testbed and the widespread use of RPL in autonomous racing, we benchmark  $\alpha$ -RPO by developing a methodology for learning competitive racing behavior with Roboracer cars. As shown in Figure 1, we emphasize the autonomy aspect by focusing on the reactive online planning case at deployment and stressing generalization for zero-shot real-world transfer.

Our key contributions are: (1) the introduction of  $\alpha$ -RPO, a novel extension of RPL; (2) which we built upon to propose an autonomous racing framework for Roboracer racing; and (3) our empirical demonstration that  $\alpha$ -RPO provides an effective inductive bias for learning competitive racing behavior with efficient real-world deployment. We see potential for widespread adoption of  $\alpha$ -RPO in other fields of robotics and facilitate further development by releasing our source code<sup>1</sup>.

## II. BACKGROUND

### A. Deep Reinforcement Learning

Let the stochastic action policy  $\pi_\theta(a|s)$ , parametrized by  $\theta$ , be used in a Markov decision process (MDP) for model-free

DRL with tuple  $(\mathcal{S}, \mathcal{A}, P, R, \gamma)$ . The policy is the mapping of observed states  $s \in \mathcal{S}$  to a probabilistic space  $\mathcal{P}(\mathcal{A})$  over the continuous actions  $a \in \mathcal{A}$ . A scalar reward  $r_t = R(s_t, a_t, s_{t+1})$  is obtained when the system transitions to a new state  $s_{t+1}$  from  $s_t$  with  $t$  denoting the timestep. The probability of transitioning to  $s_{t+1}$  is defined by  $P: \mathcal{S} \times \mathcal{A} \rightarrow \mathcal{P}(\mathcal{S})$  and  $\gamma \in (0, 1]$  is a discount factor. The expected return  $V^{\pi_\theta}(s) = \mathbb{E}_{\pi_\theta} [\sum_{l=0}^{\infty} \gamma^l r_{t+l} | s_t = s]$  is maximized by the optimal policy  $\pi_\theta^* = \arg \max_{\pi_\theta} V^{\pi_\theta}(s)$ ,  $\forall s \in \mathcal{S}$ .

In PPO [19], the stochastic action policy  $\pi_\theta(a|s)$  is parametrized by the policy network  $f_\theta(s)$  with weights  $\theta$ . This *on-policy* DRL method updates the weights  $\theta_k$  at iteration  $k$  with respect to the advantage function  $A^{\pi_{\theta_k}}(s, a) = Q^{\pi_{\theta_k}}(s, a) - V_\phi^{\pi_{\theta_k}}(s)$ . The state value  $V_\phi^{\pi_{\theta_k}}(s)$  is estimated by the critic network  $f_\phi(s)$  with weights  $\phi$ . The (clipped) PPO objective is given by

$$\mathcal{L}^P(\theta) = \mathbb{E}_{\mathcal{D}_k} [\min(\rho_t(\theta)A_t, \text{clip}(\rho_t(\theta), 1 - \epsilon, 1 + \epsilon)A_t)], \quad (1)$$

where  $A_t \equiv A^{\pi_{\theta_k}}(s_t, a_t)$ . The expectation in (1) is taken over the empirical distribution  $(s_t, a_t) \sim \mathcal{D}_k$  induced by the behavior policy  $\tilde{\pi}_{\theta_k}$  on the dataset  $\mathcal{D}_k = \{\tau_j\}$  of trajectories  $\tau_j = \{(s_t, a_t, r_t, s_{t+1})\}_{t=0}^{T-1}$  with  $T$  timesteps. Clipping the probability ratio  $\rho_t(\theta) = \frac{\pi_\theta(a_t|s_t)}{\tilde{\pi}_{\theta_k}(a_t|s_t)}$  with hyperparameter  $\epsilon$  increases training stability by limiting the divergence of the updated policy  $\pi_{\theta_{k+1}}$  from the behavior policy  $\tilde{\pi}_{\theta_k}$ . The ratio  $\rho_t$  can be interpreted as an importance sampling term, easing the on-policy requirement to update (1).

### B. Residual Policy Learning

RPL [21, 13] is a DRL paradigm that constructs the action policy  $\pi_\theta(\cdot|s)$  by fusing a static base policy  $\mu_B(s)$ , typically a classical controller, with a *learned* residual function  $f_{R,\theta}(s)$  parameterized by a deep neural network (DNN). The residual network’s weights  $\theta$  are optimized using classical DRL.

Formally, let the fused action policy  $\pi_\theta(\cdot|s)$  be a probability distribution  $D(h_\theta(s); \Lambda)$ . The distribution parameters  $h_\theta(s) \in \mathcal{H}$  are determined by a fusion map  $\mathcal{F}$ , which combines the base and the residual components according to

$$\begin{aligned} h_\theta(s) &= \mathcal{F}(\mu_B(s), f_{R,\theta}(s); \omega), \\ \pi_\theta(\cdot|s) &:= D(h_\theta(s); \Lambda), \end{aligned} \quad (2)$$

where  $\Lambda$  denotes distribution constraints, e.g., action bounds, and  $\omega \in [0, 1]$  is a *constant* mixing factor.

Several works [25, 10] instantiate  $\mathcal{F}$  as additive fusion in action space,  $a = \mu_B(s) + \omega \cdot a_R$ , where  $a_R$  is sampled from a residual distribution parameterized by  $f_{R,\theta}(s)$  or treated deterministically as the direct output. Recently, [26] showed the advantages of modeling  $D$  as a Truncated-Gaussian distribution  $\mathcal{N}_{[a,b]}(\mu, \sigma^2)$  [4]. This distribution is a *renormalized* probability density that enforces bounds  $[a, b]$  via truncation instead of hard clipping or squashing. Unlike non-linear squashing, e.g., Tanh-Gaussian, the Truncated-Gaussian guarantees *local consistency* with the base action: at zero residual mean, the mode of the fused policy  $\pi_\theta(\cdot|s)$  coincides with the base action  $\mu_B(s)$ . This ensures that the base policies’ inductive bias is correctly preserved during early training.

<sup>1</sup>Available at: [https://github.com/raphajaner/arpo\\_racing](https://github.com/raphajaner/arpo_racing).

### C. Vehicle Model Dynamics with Pacejka Tires

The state vector of a race car can be modeled as a dynamic single-track with nonlinear tire forces [10] given by

$$\mathbf{x} = [x \ y \ \delta \ v \ \psi \ \dot{\psi} \ \beta]^\top, \quad (3)$$

with the global vehicle position in  $x, y$  coordinates and vehicle orientation  $\psi$ . Moreover, the state contains the vehicle’s steering angle  $\delta$  and driving speed  $v$  in addition to the slip angle  $\beta$  and yaw rate  $\dot{\psi}$ . The model input consists of the steering velocity  $\dot{\delta}$  and longitudinal acceleration  $a$ . For the nonlinear tire model, the front and rear tire slip angles are

$$\alpha_f = \arctan \frac{-v_y - \ell_f \dot{\psi}}{v_x} + \delta, \quad \alpha_r = \arctan \frac{-v_y + \ell_r \dot{\psi}}{v_x}, \quad (4)$$

where  $\ell_f, \ell_r$  are the distances from the center of gravity to the front and rear axles. Given the normal loads  $F_{z,i}$  of the front and rear tires  $i \in \{f, r\}$ , the corresponding lateral tire forces  $F_{y,i}$  are calculated using Pacejka’s Magic Formula [18]

$$F_{y,i} = \mu D_i F_{z,i} \sin \left( C_i \arctan \left( B_i \alpha_i - E_i [B_i \alpha_i - \arctan(B_i \alpha_i)] \right) \right), \quad (5)$$

where  $\mu$  is the friction coefficient and  $(B_i, C_i, D_i, E_i)$  are tire-specific parameters. This model captures realistic driving effects such as understeering and slip in simulation.

### D. Autonomous Racing Control

Autonomous racing control methods vary in their use of prior information. Reactive methods depend solely on onboard sensing, while map-based approaches require an offline optimized racing line and accurate localization at deployment.

The FTG controller [20] is a reactive LiDAR-based method that identifies the largest collision-free gap in the scan and steers toward its center. This logic allows racing without prior maps, but its limited foresight may lead to non-optimal trajectories. The Stanley controller [24] is a map-based path-tracking algorithm that computes steering from cross-track and heading errors relative to the reference line.

## III. ATTENUATED RESIDUAL POLICY OPTIMIZATION

We propose  $\alpha$ -RPO as a straight extension of RPL that is systematically integrated into PPO. The core idea of  $\alpha$ -RPO is the fusion mechanism: unlike standard RPL, we progressively *attenuate* the influence of the base policy  $\mu_B(s)$  over the course of training until it is fully removed—only the residual network  $f_{R,\theta}(s)$  is deployed at inference time as it fully determines the action policy  $\pi_\theta(\cdot|s)$ . As shown in Algorithm 1,  $\alpha$ -RPO follows the standard PPO algorithm but leverages the PPO objective to introduce the *synchronization trick* to mitigate consistency issues caused by the attenuation.

In the following, we assume  $D$  belongs to the family of Gaussian distributions, defined by the parameters  $(\mu, \sigma) \in \mathcal{H}$ .

---

### Algorithm 1 $\alpha$ -RPO

---

```

1: for  $k = 0, 1, \dots$  do
2:   if not sync then ▷ (unsynchronized)
3:     Attenuation factor:  $\alpha_{k+1} \leftarrow \text{update\_}\alpha(k)$ 
4:     Set behavior policy  $\tilde{\pi}_{\theta_k}(\cdot|s) \leftarrow \pi_{\theta_k}(\cdot|s; \alpha_{k+1})$ 
5:   else
6:     Set behavior policy  $\tilde{\pi}_{\theta_k}(\cdot|s) \leftarrow \pi_{\theta_k}(\cdot|s; \alpha_k)$ 
7:   end if
8:   Collect  $\mathcal{D}_k$  under  $\tilde{\pi}_{\theta_k}$ ; compute  $\hat{R}_t$  and  $A^{\tilde{\pi}_{\theta_k}}(s_t, a_t)$ 
9:   if sync then ▷ (synchronized)
10:    Attenuation factor:  $\alpha_{k+1} \leftarrow \text{update\_}\alpha(k)$ 
11:   end if
12:   for epochs/minibatches do
13:     Import. sampl. ratio  $\rho_t(\theta; \alpha_{k+1}) \leftarrow \frac{\pi_\theta(a_t | s_t; \alpha_{k+1})}{\tilde{\pi}_{\theta_k}(a_t | s_t)}$ 
14:     Update policy by maximizing  $\mathcal{L}^P(\theta; \alpha_{k+1})$ 
15:     Update critic by minimizing  $\mathcal{L}^V(\phi)$ 
16:   end for
17:   Update configuration:  $\theta_{k+1} \leftarrow \theta, \phi_{k+1} \leftarrow \phi$ 
18: end for

```

---

### A. Policy Fusion

The policy fusion in  $\alpha$ -RPO extends (2) by introducing the *iteration-dependent* attenuation factor  $\alpha \in [0, 1]$

$$h_\theta(s; \alpha) = \mathcal{F}(\mu_B(s), f_{R,\theta}(s); \alpha) \quad (6)$$

$$\pi_\theta(\cdot|s; \alpha) := D(h_\theta(s; \alpha); \Lambda),$$

to control the base policy’s influence on the policy  $\pi_\theta(\cdot|s; \alpha)$  by defining the distribution’s parameters as

$$\begin{aligned} \mu &:= \mu_\theta(s) = (1 - \alpha) \cdot \mu_B(s) + \max(\alpha, \alpha_{\text{init}}) \cdot f_{R,\theta}(s) \\ \sigma &:= \sigma_\theta(s) = \exp(f'_{R,\theta}(s)) \quad (f' \text{ uses a separate head}). \end{aligned} \quad (7)$$

The constant coefficient  $\alpha_{\text{init}} \in [0, 1]$  sets the initial scaling of the residual network. We update  $\alpha$  using a linear schedule

$$\text{update\_}\alpha(k) = \min \left\{ 1, \frac{k}{K_{\text{end}}} \right\}, \quad (8)$$

where  $K_{\text{end}}$  denotes the iteration after which the base policy is fully phased out. Given  $\alpha \approx 0$  at the beginning of training and due to weight initialization, the agent primarily follows the base policy since  $\mathbb{E}[f_{R,\theta}(s)] \approx 0$ . As training progresses and  $\alpha$  increases towards 1, the residual network  $f_{R,\theta}(s)$  gradually replaces  $\mu_B$  until it becomes fully attenuated at  $\alpha = 1$ .

### B. Synchronization Trick

As shown in Algorithm 1, naïvely updating  $\alpha$  (lines 2–4) alters the behavior policy before data collection. Since the policy  $\pi_\theta(\cdot|s; \alpha)$  is explicitly conditioned on  $\alpha$ , and the residual network is agnostic to the external modification of the base policy’s influence, this creates a *consistency* issue. Specifically, if the behavior policy  $\tilde{\pi}_{\theta_k} \leftarrow \pi_{\theta_k}(\cdot|s; \alpha_{k+1})$  uses the updated attenuation factor  $\alpha_{k+1}$  when interacting with the environment, the sampled actions and probabilities diverge unintentionally from the original policy  $\pi_{\theta_k}(\cdot|s; \alpha_k)$ , which resulted from the previous parameter update (line 17).

We mitigate this issue in  $\alpha$ -RPO by proposing the *synchronization trick* (lines 9–11): we use the behavior policy  $\tilde{\pi}_{\theta_k} \leftarrow \pi_{\theta_k}(\cdot|s; \alpha_k)$  to collect rollouts and calculate advantages while keeping  $\alpha_k$  constant. Only after data collection is  $\alpha$  updated to  $\alpha_{k+1}$ , immediately before the optimization loop. This ensures that the shifted influence of the base policy is implicitly absorbed into the importance sampling-based update of  $\theta_k$  in PPO. This relies on the property that, due to the clipped importance sampling ratio  $\rho_t$ , PPO tolerates mild off-policy updates, i.e., the loss can be computed using rollouts collected from  $\tilde{\pi}_{\theta_k}$  using  $\alpha_k$  while optimizing the target policy  $\pi_\theta$  using  $\alpha_{k+1}$ . Consequently, this synchronization enables the unbiased use of the current policy for data collection while ensuring correct advantage calculation.

#### IV. AUTONOMOUS RACING FRAMEWORK

In this section, we develop an autonomous racing framework to demonstrate the efficacy of our proposed  $\alpha$ -RPO method. We build our framework upon the Roboracer platform, a popular real-world autonomous racing series [17, 7]. Our  $\alpha$ -RPO agent is trained in simulation for the autonomous control of a Roboracer car—with the goal of efficient, zero-shot transfer of the agent to the real-world platform after training.

##### A. Racing Environment

1) *Real-World Platform*: As shown in Figure 1, the Roboracer platform utilizes 1:10-scale remote-control cars, equipped with a 2D LiDAR. This sensor enables the car to perceive its environment through distance measurements; in this case, to the racetrack walls. The resulting scan  $L_t \in \mathcal{R}^{1081}$  cover a field-of-view (FOV) of  $270^\circ$  and are obtained at 40 Hz. The cars are also equipped with an IMU sensor, allowing for direct measurement of the yaw rate  $\dot{\psi}_t$ . The longitudinal speed  $v_t^{\text{long}}$  is estimated based on the motor position. The car’s control action  $a = [\delta, v]$  consists of steering angle  $\delta$  and target speed  $v$  as input to the car’s low-level controller.

2) *Simulation*: We use a custom version of the Roboracer gym [17] with improved dynamics as simulator, based on the single-track model with the non-linear Pacejka tire model as discussed in Section II-C. The used tire coefficients are realistic estimates, but without real-world identification. We set the maximum vehicle speed to  $8.0 \text{ m s}^{-1}$ . The observation and control frequencies are fixed to 40 Hz, same as the real-world Roboracer’s. Sensor noise is simulated for the LiDAR scan, speed, and yaw rate measurements as Gaussian noise.

##### B. $\alpha$ -RPO Agent

We adopt [26] and set the policy distribution  $D$  in (6) as a Truncated-Gaussian  $\mathcal{N}_{[-1,1]}(\mu, \sigma^2)$ . The base and residual modules of the  $\alpha$ -RPO agent are:

- *Base Module*: Our default base module uses the Stanley controller as base policy  $\mu_B(s)$  and outputs the base action  $a_B = [\delta_B, v_B]$ . When using standard RPL, this controller would require localization during deployment. In contrast,  $\alpha$ -RPO leads to a fully *reactive* controller design, as the base policy is fully phased out by the end of

training; position information is readily available during training. We also ablate using a FTG controller instead. See Section II-D for a description of the controllers.

- *Residual Module*: The residual network  $f_{R,\theta}(s)$  with weights  $\theta$  parametrizes the state-dependent location  $\mu_\theta(s)$  and scale  $\sigma_\theta(s)$  according to (7).

1) *State and Action Space*: Using only measurements of on-board sensors available on the real-world platform, we define observations  $o_t$  at time  $t$  as

$$o_t = [L'_t \quad a_{t-1} \quad v_t^{\text{long}} \quad \dot{\psi}_t]^\top, \quad (9)$$

with the preprocessed LiDAR scan  $L'_t$  as the main modality. The raw scans  $L_t \in \mathcal{R}^{1081}$  are preprocessed by cropping the vector to the central 1,024 readings and normalized to  $[0, 1]$ . The normalized vector is downsampled using average pooling with a kernel size and stride of 2, resulting in the output vector  $L'_t \in [0, 1]^{512}$ . To embed temporal information, we define the current state  $s_t \in \mathcal{S}$  as a stack of  $n_f = 4$  consecutive observations  $s_t := (o_{t-n_f+1}, \dots, o_t)$ .

After obtaining the fused policy  $\pi_\theta(\cdot|s)$ , the target steering and speed are sampled  $a_t \sim \pi_\theta(\cdot|s)$ , resulting in bounded values  $a_t' \in [-1, 1]$  due to the used Truncated-Gaussian distribution. These values are rescaled to the vehicle’s physical action limits to form  $a_t \in \mathcal{A}$ .

2) *Reward Formulation*: We use the progress along the centerline  $d_t^c$  as the main optimization target, i.e., the distance between projections of the car’s position onto the centerline at subsequent timesteps. In addition, our reward function

$$r_t = 0.1 \cdot d_{t+1}^c - 0.001 \cdot |\delta_{t+1} - \delta_t| - 5 \cdot \mathbf{1}_c, \quad (10)$$

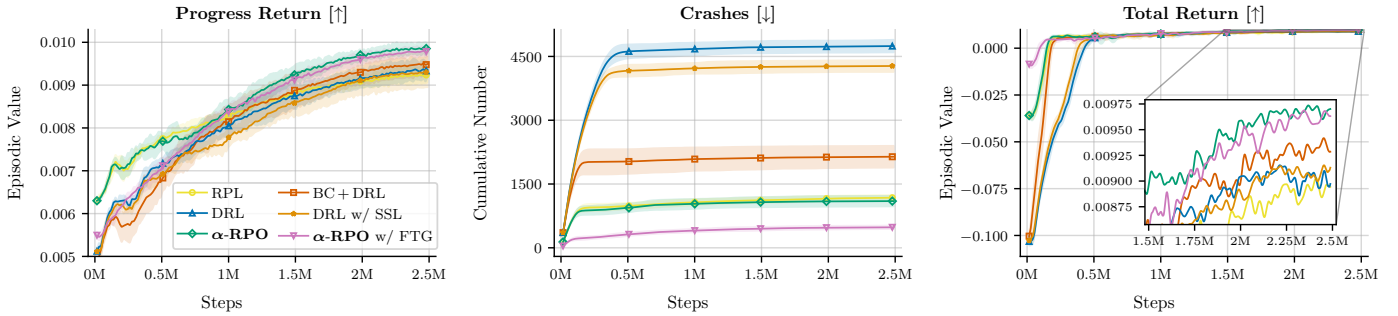
penalizes large steering action changes between time steps and contains a penalty with  $\mathbf{1}_c = 1$  for collisions with the walls.

3) *Attenuation Schedule*: The attenuation factor  $\alpha$  is scheduled using (8) with  $K_{\text{end}}$  set to 25 % of the total training steps. The initial scaling factor is set to  $\alpha_{\text{init}} = 1$ , meaning that the base policy decreases gradually during training while the residual network scaling remains constant.

4) *Neural Network Architecture*: We employ a DNN architecture comprising a shared encoder with separate heads for the residual network  $f_{R,\theta}$  and critic network  $f_\phi$ , totaling 344,357 trainable parameters. The LiDAR encoder processes  $L'_t$  by a stack of five 1D convolutional layers. To extract a compact feature representation from the convolutional feature maps, we apply a SpatialSoftmax layer [8] followed by Linear projection, yielding the final LiDAR embedding  $z_t \in \mathbb{R}^{128}$ . The embedding  $z_t$  is concatenated with the encoded vehicle states  $h_t$  and normalized via LayerNorm in the Fusion Block. This fused feature vector serves as the input to the independent fully connected layers of the actor and critic heads. Appendix D contains a visualization of this DNN.

#### V. EXPERIMENTS

We use the presented autonomous racing framework to evaluate the performance of our proposed  $\alpha$ -RPO method. We first discuss simulation results, as this allows a detailed comparison to other methods. Eventually, we zero-shot transfer



(a) Return corresponding to the reward for lap progress  $d_{t+1}^{\text{cl}}$  of (10).

(b) Cumulative number of crashes with the racetrack walls during training.

(c) Total return; the zoomed figure shows the last 1M steps in detail.

Fig. 2: Learning curves with the episodic values of the return during training, showing both the fraction of the return corresponding only to the lap progress (left) and the total sum (right). Additionally, the cumulative number of crashes during training is shown (mid). The agents are trained for 2.5M interaction steps on 15 different maps.

the agents trained with  $\alpha$ -RPO to the real world and conduct a study on a real-world racetrack using a Roboracer car.

1) *Training*: We run training for 2.5M timesteps, using 15 parallel environments to collect trajectories of 1024 timesteps. Due to the high efficiency of the methodology and parallelized training, full training takes *less than 15 min* on a workstation with an AMD Ryzen 9 9950X CPU and an NVIDIA GeForce RTX 5090 GPU. We ensure reproducibility by listing simulation parameters and hyperparameters of PPO in Appendix A.

2) *Racetracks*: Our pipeline uses 15 synthetically generated racetracks during training. Additionally, another 6 racetracks are used for testing generalization: 5 are also synthetically generated, while the *Munich* racetrack is the SLAM-based map of our own *real-world* racetrack. Renderings of all racetracks are presented in Appendix B.

3) *Evaluation*: We evaluate on against-the-clock races that finish after completion of 5 laps. Like in the Roboracer competitions, if a crash happens during evaluation, (1) the race is stopped and the car is relocated to the nearest point on the centerline, (2) a 5-second penalty is added to the lap time, and (3) the race resumes. Per-racetrack results are averaged over 10 different starting positions on the track. Unless otherwise stated, our presented results are mean values from 5 independent training runs with different seeds, and shaded areas show the corresponding standard deviation.

4) *Baselines*: To provide comprehensive results, we include results from multiple related learning-based baseline methods: (1) standard RPL, (2) standard DRL, (3) DRL with BC-based pretraining of the actor using a recorded dataset of Stanley-based trajectories of 0.5M steps, and (4) DRL with an additional self-supervised learning (SSL) for distilling the base action during training. All these methods use PPO with the same configuration as  $\alpha$ -RPO. Additionally, the two classical controllers, (5) FTG and (6) Stanley, are evaluated to provide a better perspective on the learning-based methods. Both controllers use a single set of parameters optimized for robustness to prevent collisions across all training racetracks, which may result in increased lap times on individual tracks.

### A. Benchmark

1) *Training Curves*: We evaluate the training curves of  $\alpha$ -RPO in comparison to the baselines, visualizing first the reward corresponding to the *progress*  $d_{t+1}^{\text{cl}}$  of (10) as this is the best indicator of how fast the agents have learned to race. As expected, Figure 2a shows that using a base policy is a strong inductive bias that bootstraps early learning in  $\alpha$ -RPO and RPL as the vehicle *can drive* directly when learning starts. We see that  $\alpha$ -RPO and RPL initially perform very similarly for 0.6M steps. After a short phase of instability,  $\alpha$ -RPO gains an edge in performance after approx. 0.8M steps, eventually achieving the highest average progress of 0.99. This result supports the hypothesis that the base policy is only a meaningful inductive bias in early training but hinders optimal final performance, as RPL agents must continuously override the base policy’s behavior. As a result, after full training, DRL and RPL perform almost identically<sup>2</sup>.

Additionally, our results show that DRL-based methods can outperform RPL when using BC-based pretraining for the agent or adding a SSL loss during training. This reiterates our aforementioned hypothesis that using the base policy in RPL is primarily useful during early training but may lead to lower final performance. The additional result of  $\alpha$ -RPO w/ FTG demonstrates that, while  $\alpha$ -RPO benefits from the faster Stanley base policy, the learning paradigm provides a general improvement over all baselines. The results in Figure 2b, which show the cumulative number of crashes during training, confirm this aspect since the DRL-based methods exhibit a substantially higher collision count during training. In contrast, both RPL and  $\alpha$ -RPO sustain less than 1,500 total collisions during training; BC-pretraining is also effective at reducing the large amount of collisions during the early learning phase. Notably, the  $\alpha$ -RPO agent using the FTG base policy causes fewer than 500 total crashes, likely since the Stanley already operates at a higher racing speed during exploration.

<sup>2</sup>It is noteworthy that DRL itself also starts with non-zero progress as an inductive bias arises from the action space definition itself, leading to an expected speed target of  $4 \text{ m s}^{-1}$  at initialization.

TABLE I: Simulated racing results, showing a subset of 7 training and 6 testing racetracks. The *Munich* racetrack is an SLAM-based map of our own real-world racetrack. A race finishes when 5 laps are completed. The acronym BCD is short for the BC+DRL method. Full results including all maps and DRL+SSL are shown in Appendix C.

Racetrack	Total race time [↓]						Collisions per lap [↓]						Maximum speed [↑]						
	FTG	Stanley	DRL	BCD	RPL	$\alpha$ -RPO	FTG	Stanley	DRL	BCD	RPL	$\alpha$ -RPO	FTG	Stanley	DRL	BCD	RPL	$\alpha$ -RPO	
<b>Train</b>																			
Abu Dhabi	67.54	50.41	48.50	46.29	48.16	44.02	0.00	0.00	0.03	0.00	0.09	0.00	4.32	5.06	4.81	4.72	5.15	5.15	
London	71.04	55.72	55.73	50.05	52.57	47.58	0.00	0.00	0.20	0.00	0.04	0.00	5.03	4.81	5.00	4.84	5.10	5.29	
Mexico City	55.78	41.15	37.51	37.54	37.78	35.53	0.04	0.00	0.00	0.00	0.00	0.00	4.78	5.21	5.10	4.92	5.37	5.50	
New York	71.88	63.08	54.49	54.00	56.17	51.95	0.00	0.00	0.00	0.00	0.00	0.00	4.58	4.45	5.08	4.95	4.89	5.34	
Paris	51.40	39.74	41.08	35.88	35.78	34.13	0.00	0.00	0.19	0.00	0.00	0.00	4.48	5.32	5.25	5.00	5.41	5.50	
Sydney	55.95	44.52	40.18	40.16	40.43	38.37	0.00	0.00	0.00	0.00	0.00	0.00	4.94	4.98	5.23	4.91	5.38	5.44	
...																			
Average Train	67.74	53.85	49.92	48.31	49.84	<b>46.24</b>	0.01	<b>0.00</b>	0.04	0.00	0.01	<b>0.00</b>	4.70	5.00	5.10	4.93	5.17	<b>5.41</b>	
<b>Test</b>																			
Buenos Aires	67.29	52.33	49.79	49.09	50.30	47.30	0.00	0.00	0.00	0.00	0.00	0.00	4.40	4.85	4.90	4.86	4.88	5.24	
Istanbul	69.62	52.27	48.15	53.01	86.42	45.86	0.00	0.00	0.00	0.19	1.24	0.00	4.48	5.32	4.95	4.82	5.30	5.29	
Madrid	66.91	53.51	49.66	49.09	50.87	47.28	0.00	0.00	0.00	0.00	0.00	0.00	4.97	4.46	5.03	4.88	4.79	5.32	
Seoul	77.78	65.95	61.57	59.96	65.19	57.76	0.00	0.00	0.00	0.00	0.08	0.00	4.94	5.03	5.21	5.00	5.10	5.43	
Toronto	76.31	65.20	59.63	57.92	62.67	55.58	0.00	0.00	0.00	0.00	0.00	0.00	5.18	4.60	5.16	4.95	4.95	5.35	
<i>Munich</i>	38.10	32.77	41.87	33.60	32.71	28.91	0.00	0.00	0.41	0.14	0.01	0.00	3.41	4.29	4.69	4.70	4.46	4.92	
Average Test	66.00	53.67	51.78	50.44	58.03	<b>47.11</b>	<b>0.00</b>	<b>0.00</b>	0.07	0.06	0.22	<b>0.00</b>	4.57	4.76	4.99	4.87	4.92	<b>5.26</b>	

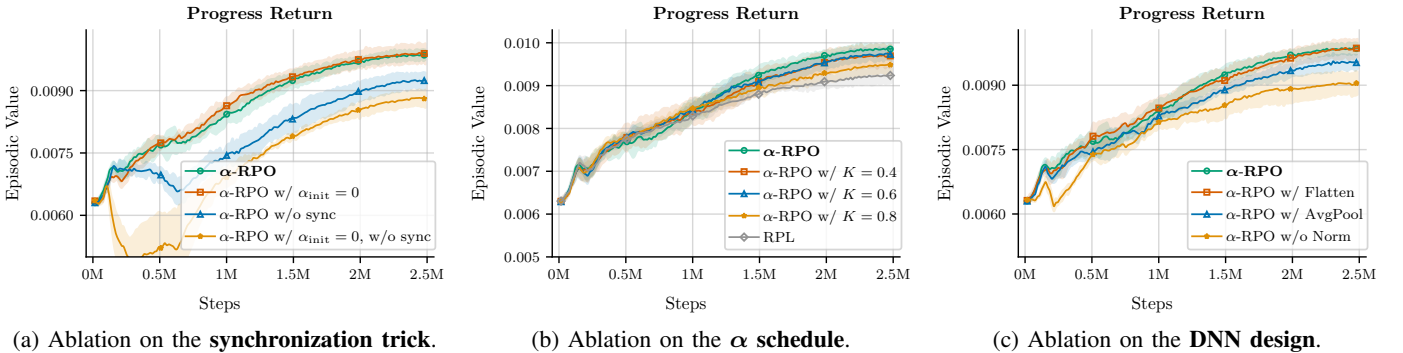


Fig. 3: Learning curves showing the progress-return for our ablation studies. We ablate the synchronization trick (left), longer  $\alpha$ -schedules (mid), and design aspects of the DNN (right).

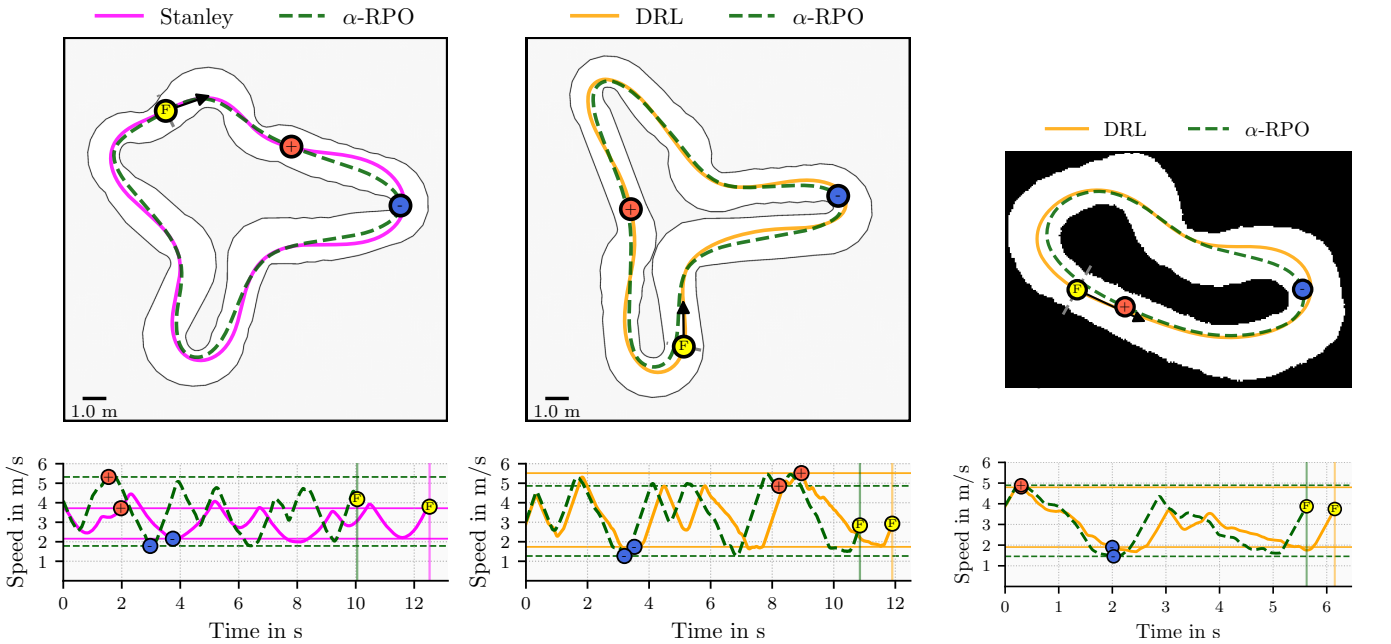
In general, it can be seen that  $\alpha$ -RPO leverages the advantages of RPL during early training but is capable of higher final performance after attenuation of the base policy. As such, we understand  $\alpha$ -RPO as a form of guided exploration which helps to bootstrap DRL learning.

2) *Lap Results*: Table I summarizes the performance of  $\alpha$ -RPO against the baselines.  $\alpha$ -RPO consistently outperforms all other methods, achieving the lowest average total race time of 46.24s on training and 47.11s on unseen test tracks. Notably,  $\alpha$ -RPO demonstrates superior generalization capabilities compared to standard RPL. While standard RPL degrades significantly on unseen tracks to an average of 58.03s with 0.22 collisions per lap,  $\alpha$ -RPO maintains robust performance with zero collisions. Furthermore, the maximum velocity indicates that  $\alpha$ -RPO races closer to the physical limit, reaching the highest average max speed of 5.41 m s<sup>-1</sup>. While the BC+DRL method has learned to prevent all collisions during training, the agent shows lower generalization capabilities than  $\alpha$ -RPO. On our own real-world-based racetrack, *Munich*,  $\alpha$ -RPO improves lap times by over 12% compared to Stanley, indicating strong potential for effective sim-to-real transfer.

## B. Ablation Studies

We validate our design choices through detailed ablations, focusing on the progress return as performance measure.

- Figure 3a confirms the necessity of our *synchronization trick*; it stabilizes training and is a key contribution of  $\alpha$ -RPO. The effectiveness of leveraging the importance sampling (IS) term in (1) to reduce the bias when changing the attenuation factor is even more apparent when setting  $\alpha_{init} = 0$ . Here, the residual network’s scale also changes continuously during the attenuation phase, leading to substantial instability without synchronization.
- Figure 3b demonstrates that *shorter* attenuation schedules are advantageous: the longer the attenuation, the closer the agent’s performance to standard RPL.
- The architectural analysis in Figure 3c identifies the fusion block’s LayerNorm for feature normalization as a vital component. Using a SpatialSoftmax layer [8] also has advantages: it reduces the feature space and total number of parameters compared to Flatten, but performs better than AveragePooling [27] for feature reduction, presumably due to the centered nature of the observation.



(a) Stanley (magenta) against  $\alpha$ -RPO (green) on the New York racetrack (training). (b) DRL (orange) against  $\alpha$ -RPO (green) on the Toronto racetrack (testing). (c) DRL (orange) against  $\alpha$ -RPO (green) on the Munich racetrack (testing).

Fig. 4: Qualitative comparison of trajectories (**top**) and speed profiles (**bottom**) on three racetracks, showing a single flying lap. Markers indicate a specific point-of-interest (POI) on the racetracks: + marks a high-speed section (red), - indicates the section with minimal speed (blue), while F is the finish line (yellow).

### C. Qualitative Analysis of Trajectories

To better understand the performance gains, we analyze the resulting trajectories and speed profiles on three representative maps in the following. It is apparent from Figure 4a that the racing line used for the Stanley controller is based on minimum-curvature optimization. The learned trajectory of  $\alpha$ -RPO follows a similar shape; however, the path length is substantially shortened in several sections by following the inner wall more closely for a straighter path. As seen at + marked section, this behavior allows the agent to achieve a higher maximum speed exceeding  $5 \text{ m s}^{-1}$ .

Figure 4b and 4c compare  $\alpha$ -RPO against the DRL baseline on unseen test tracks. On the *Toronto* racetrack, DRL cannot find the line that cuts corners as aggressively as  $\alpha$ -RPO does. The speed profile shows that  $\alpha$ -RPO can accelerate to higher speeds while braking harder, resulting in the significant lap-time reduction. Similar behavior is evident on the *Munich* track, where  $\alpha$ -RPO brakes harder at the curve with minimum speed, which allows the agent to turn in harder, thus having a straighter line to accelerate out of the corner.

### D. Fine-Tuning on Single Racetracks

We explore the capabilities of  $\alpha$ -RPO agents to fine-tune on a single new racetrack after initial training focused on generalization across the 15 training maps. Such fine-tuning is highly relevant to real-world racing in Roboracer competitions, as it allows for *pre-training* an agent that is then fine-tuned once the competition’s racetrack is accessible. We conduct the

TABLE II: Results for fine-tuned agents of the single best training seed, denoted by \*. Fine-tuning continues training only on the specific racetrack for a further 0.5 M interaction steps.

Racetrack	Total race time in s [ $\downarrow$ ]			
	DRL	DRL*	$\alpha$ -RPO	$\alpha$ -RPO*
Toronto	59.95	59.37	54.90	<b>52.49</b>
Madrid	50.30	47.40	46.59	<b>43.41</b>
Munich	31.23	29.43	28.52	<b>26.35</b>

fine-tuning by continuing training for 0.5M interaction steps on a single racetrack<sup>3</sup>. The results in Table II substantiate that single-track fine-tuning on new maps leads to a meaningful performance increase; however, DRL still lags behind  $\alpha$ -RPO.

### E. Real World Experiments

1) *Deployment*: The design of  $\alpha$ -RPO offers significant advantages for real-world deployment, as only a standalone DNN is required. This case allows for very low inference times [9, 29] and *removes* the need for complex system integration with the base policy. Our Roboracer’s onboard embedded board is an NVIDIA Jetson Orin Nano Super, which enables efficient DNN acceleration via GPU cores. During deployment of our  $\alpha$ -RPO agent on the Roboracer car, we measure average inference latencies of 3.5 ms, including the *full* LiDAR preprocessing and ROS2-based topic publishing

<sup>3</sup>We achieved the best results when reducing the initial learning rate to  $5e^{-5}$  and collecting data from only 4 parallel environments.

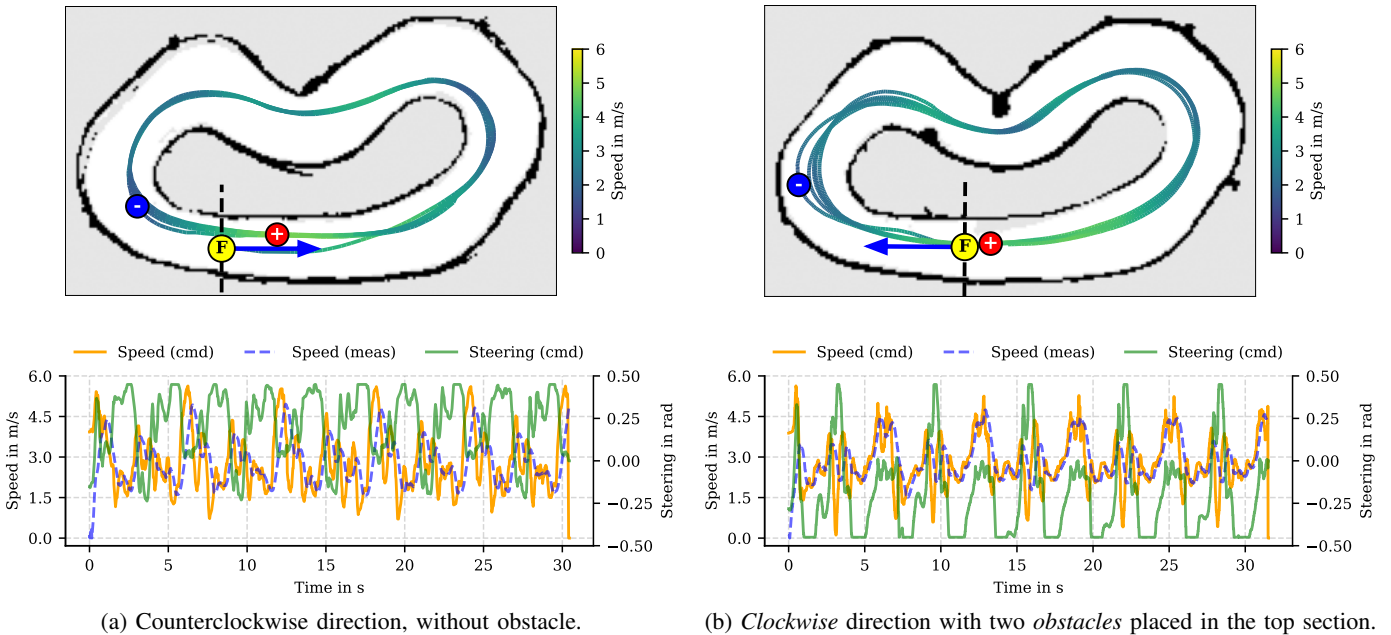


Fig. 5: Real-world trajectories of  $\alpha$ -RPO on the *Munich* racetrack for 5 laps (**top**), including a variation with two obstacles placed; current speed shown as color bar. Positions are estimated offline from `rosbag` data using SLAM. The agent’s actions command (cmd) and measured speed (meas.) are also shown (**bottom**). Markers indicate a specific POI on the racetracks: + marks a high-speed section (red), – indicates the section with minimal speed (blue), while F is the finish line (yellow).

stack. In contrast, a well-optimized localization-based stack is reported by Baumann et al. [2] with an average of 7.5 ms, even if running on an Intel i5-10210U. Moreover,  $\alpha$ -RPO enables a form of *privileged* learning since we do not need to deploy the Stanley controller that was used as base policy; RPL and hybrid approaches [9] would still include heavy computational overhead due to the required localization.

2) *Zero-Shot Real-World Transfer*: We visualize recorded real-world trajectories in Figure 5a, where we tested an agent on our own *Munich* racetrack. Although *Munich* was not used during training, our  $\alpha$ -RPO successfully bridges the sim-to-real gap and generalizes to this new racetrack. It can be seen that the agent consistently chooses the same trajectory, following the inside wall closely. The measured *real-world* racing results are shown in Table III. Compared to simulated results,  $\alpha$ -RPO achieves a similarly high maximum speed of approx.  $5.0 \text{ m s}^{-1}$  during real-world deployment, but the average single lap duration increases by approx. 0.4 s.

We stress the robustness of  $\alpha$ -RPO in Figure 5b, placing two static *obstacles* on the racetrack. The agent adjusts its trajectory smoothly to avoid a collision with the obstacle. While these results demonstrate robustness of the  $\alpha$ -RPO agent, they indicate a certain degree of simulation mismatch; for example, there is motor stuttering during the start-up in the first 1.5 s, requiring the agent to brake hard in this corner. In general, the figures highlight that driving behavior and collision avoidance are consistent and repeatable. Please find the video material of these experiments in the Supplementary.

TABLE III: Real-world lap times on the Munich track, using the model corresponding to the best seed of each method. Finish times cover races with 5 full laps. Reported values are estimated offline from `rosbag` data.

Metric	Method			
	FTG	DRL	$\alpha$ -RPO	$\alpha$ -RPO*
Finishing time in s [ $\downarrow$ ]	40.2	34.4	<b>30.5</b>	28.1
Difference to simulation in s [ $\downarrow$ ]	+2.1	+3.2	<b>+2.0</b>	+1.7
Maximum speed in $\text{m s}^{-1}$ [ $\uparrow$ ]	3.1	4.8	<b>5.0</b>	5.4

## VI. LIMITATIONS AND FUTURE WORK

Unlike RPL approaches that use a base policy to provide safety guarantees [5],  $\alpha$ -RPO yields a non-verifiable neural policy. While our results support this standalone deployment, the agent forfeits the explicit, verifiable constraints inherent in classical control, hindering formal verification. Additionally, our simulation parameters were empirically calibrated rather than validated via rigorous system identification. Although zero-shot transfer was successful, unmodeled dynamic effects seemingly still hinder performance at the limits of handling. Since our fine-tuning experiment assessed strong effectiveness, we envision an online, real-world fine-tuning procedure for future work. Furthermore,  $\alpha$ -RPO may remain sensitive to the quality of the base policy and the linear attenuation schedule of  $\alpha$ . An ablation should aim to better understand this relation by testing various base policies and schedules. Eventually, future work should extend the usage of  $\alpha$ -RPO to other robotic control domains to assess its broader applicability.

## VII. CONCLUSION

This work introduces  $\alpha$ -RPO, an extension of the popular RPL training paradigm. In contrast to classical RPL, our proposed method progressively attenuates the base policy during training, thereby improving performance by removing the ambiguity between the base and residual policies. We build an autonomous racing methodology upon  $\alpha$ -RPO for 1:10-scaled autonomous racing to evaluate  $\alpha$ -RPO under challenging conditions. In both simulation and zero-shot real-world transfer to Roboracer cars,  $\alpha$ -RPO achieves robust, competitive racing behavior. We confirm that our proposed synchronization trick substantially stabilizes training. Moreover, our results demonstrate  $\alpha$ -RPO's practicality for real-world robotic deployment as  $\alpha$ -RPO yields a standalone neural policy after training, which enables simplified, efficient real-world deployment with low inference time.

## ACKNOWLEDGMENTS

Marco Caccamo was supported by an Alexander von Humboldt Professorship endowed by the German Federal Ministry of Education and Research.

## REFERENCES

- [1] Mohammadamin Barekatain, Ryo Yonetani, and Masashi Hamaya. Multipolar: multi-source policy aggregation for transfer reinforcement learning between diverse environmental dynamics. In *Int. Conf. on Artificial Intelligence*, pages 3108–3116, 2021.
- [2] Nicolas Baumann, Edoardo Ghignone, Jonas Kühne, Niklas Bastuck, Jonathan Becker, Nadine Imholz, Tobias Kränzlin, Tian Yi Lim, Michael Lötscher, Luca Schwarzenbach, et al. Forzaeth race stack—scaled autonomous head-to-head racing on fully commercial off-the-shelf hardware. *Journal of Field Robotics*, 42(4): 1037–1079, 2025.
- [3] Johannes Betz, Hongrui Zheng, Alexander Liniger, Ugo Rosolia, Phillip Karle, Madhur Behl, Venkat Krovi, and Rahul Mangharam. Autonomous vehicles on the edge: A survey on autonomous vehicle racing. *IEEE Open Journal of Intelligent Transportation Systems*, 3:458–488, 2022.
- [4] John Burkardt. The truncated normal distribution. *Department of Scientific Computing Website, Florida State University*, 1(35):58, 2014.
- [5] Hongpeng Cao, Yanbing Mao, Lui Sha, and Marco Caccamo. Physics-regulated deep reinforcement learning: Invariant embeddings. In *Int. Conf. on Learning Representations*, 2024.
- [6] Benjamin Evans, Herman A Engelbrecht, and Hendrik W Jordaan. Learning the subsystem of local planning for autonomous racing. In *Int. Conf. on Robotics and Automation*, pages 601–606. IEEE, 2021.
- [7] Benjamin David Evans, Raphael Trumpp, Marco Caccamo, Felix Jahncke, Johannes Betz, Hendrik Willem Jordaan, and Herman Arnold Engelbrecht. Unifying fltenth autonomous racing: Survey, methods and benchmarks. *arXiv preprint arXiv:2402.18558*, 2024.
- [8] Chelsea Finn, Xin Yu Tan, Yan Duan, Trevor Darrell, Sergey Levine, and Pieter Abbeel. Deep spatial autoencoders for visuomotor learning. In *Int. Conf. on Robotics and Automation*, pages 512–519. IEEE, 2016.
- [9] Edoardo Ghignone, Nicolas Baumann, and Michele Magno. Tc-driver: A trajectory-conditioned reinforcement learning approach to zero-shot autonomous racing. *IEEE Transactions on Field Robotics*, 1:527–536, 2024.
- [10] Edoardo Ghignone, Nicolas Baumann, Cheng Hu, Jonathan Wang, Lei Xie, Andrea Carron, and Michele Magno. Rlpp: A residual method for zero-shot real-world autonomous racing on scaled platforms. In *Int. Conf. on Robotics and Automation*, pages 16664–16670, 2025.
- [11] Benedict Hildisch, Edoardo Ghignone, Nicolas Baumann, Cheng Hu, Andrea Carron, and Michele Magno. Drive fast, learn faster: On-board RL for high performance autonomous racing. *Reinforcement Learning Journal*, 6:829–861, 2025.
- [12] Ziyue Huang, Haoqi Yuan, Yuhui Fu, and Zongqing Lu. Efficient residual learning with mixture-of-experts for universal dexterous grasping. In *Int. Conf. on Learning Representations*, 2025.
- [13] Tobias Johannink, Shikhar Bahl, Ashvin Nair, Jianlan Luo, Avinash Kumar, Matthias Loskyll, Juan Aparicio Ojea, Eugen Solowjow, and Sergey Levine. Residual reinforcement learning for robot control. In *Int. Conf. on Robotics and Automation*, pages 6023–6029. IEEE, 2019.
- [14] Zhongyu Li, Xuxin Cheng, Xue Bin Peng, Pieter Abbeel, Sergey Levine, Glen Berseth, and Koushil Sreenath. Reinforcement learning for robust parameterized locomotion control of bipedal robots. In *Int. Conf. on Robotics and Automation*, pages 2811–2817. IEEE, 2021.
- [15] Volodymyr Mnih, Koray Kavukcuoglu, David Silver, Andrei A Rusu, Joel Veness, Marc G Bellemare, Alex Graves, Martin Riedmiller, Andreas K Fidjeland, Georg Ostrovski, et al. Human-level control through deep reinforcement learning. *nature*, 518(7540):529–533, 2015.
- [16] Mohammadreza Nakhaei, Aidan Scannell, and Joni Pajarinen. Residual learning and context encoding for adaptive offline-to-online reinforcement learning. In *6th Annual Learning for Dynamics & Control Conference*, pages 1107–1121. PMLR, 2024.
- [17] Matthew O’Kelly, Hongrui Zheng, Dhruv Karthik, and Rahul Mangharam. Fltenth: An open-source evaluation environment for continuous control and reinforcement learning. In *NeurIPS 2019 Competition and Demonstration Track*, pages 77–89. PMLR, 2020.
- [18] HB Pacejka and IJM Besselink. Magic formula tyre model with transient properties. *Vehicle system dynamics*, 27(S1):234–249, 1997.
- [19] John Schulman, Filip Wolski, Prafulla Dhariwal, Alec Radford, and Oleg Klimov. Proximal policy optimization algorithms. *arXiv preprint arXiv:1707.06347v2*, 2017.

- [20] Volkan Sezer and Metin Gokasan. A novel obstacle avoidance algorithm: “follow the gap method”. *Robotics and Autonomous Systems*, 60(9):1123–1134, 2012.
- [21] Tom Silver, Kelsey Allen, Josh Tenenbaum, and Leslie Kaelbling. Residual policy learning. *arXiv preprint arXiv:1812.06298*, 2018.
- [22] Kyle Stachowicz, Dhruv Shah, Arjun Bhorkar, Ilya Kostrikov, and Sergey Levine. Fastrlap: A system for learning high-speed driving via deep rl and autonomous practicing. In *Conf. on Robot Learning*, pages 3100–3111. PMLR, 2023.
- [23] Chen Tang, Ben Abbatematteo, Jiaheng Hu, Rohan Chandra, Roberto Martín-Martín, and Peter Stone. Deep reinforcement learning for robotics: A survey of real-world successes. In *Proc. of the AAAI Conference on Artificial Intelligence (AAAI)*, volume 39, pages 28694–28698, 2025.
- [24] Sebastian Thrun, Mike Montemerlo, Hendrik Dahlkamp, David Stavens, Andrei Aron, James Diebel, Philip Fong, John Gale, Morgan Halpenny, Gabriel Hoffmann, et al. Stanley: The robot that won the darpa grand challenge. *Journal of Field Robotics*, 23(9):661–692, 2006.
- [25] Raphael Trumpp, Denis Hoornaert, and Marco Caccamo. Residual policy learning for vehicle control of autonomous racing cars. In *IEEE Intelligent Vehicles Symposium*, pages 1–6. IEEE, 2023.
- [26] Raphael Trumpp, Ehsan Javanmardi, Jin Nakazato, Manabu Tsukada, and Marco Caccamo. Racemop: Mapless online path planning for multi-agent autonomous racing using residual policy learning. In *Int. Conf. on Intelligent Robots and Systems*, pages 8449–8456. IEEE, 2024.
- [27] Raphael Trumpp, Ansgar Schäfftlein, Mirco Theile, and Marco Caccamo. Impoola: The power of average pooling for image-based deep reinforcement learning. *Reinforcement Learning Journal*, 6:1025–1047, 2025.
- [28] Jiaxu Xing, Angel Romero, Leonard Bauersfeld, and Davide Scaramuzza. Bootstrapping reinforcement learning with imitation for vision-based agile flight. In *Conf. on Robot Learning*, pages 2542–2556. PMLR, 2025.
- [29] Mohammed Misbah Zarrar, Qitao Weng, Bakhbyrgyen Yerjan, Ahmet Soyyigit, and Heechul Yun. Tinylidarnet: 2d lidar-based end-to-end deep learning model for f1tenth autonomous racing. In *Int. Conf. on Intelligent Robots and Systems*, pages 2878–2884. IEEE, 2024.
- [30] Ruiqi Zhang, Jing Hou, Guang Chen, Zhijun Li, Jianxiao Chen, and Alois Knoll. Residual policy learning facilitates efficient model-free autonomous racing. *IEEE Robotics and Automation Letters*, 7(4):11625–11632, 2022.
- [31] Ruiqi Zhang, Dingqi Zhang, and Mark W Mueller. Prox-fly: Robust control for close proximity quadcopter flight via residual reinforcement learning. In *Int. Conf. on Robotics and Automation*, pages 13683–13689. IEEE, 2025.

APPENDIX A  
REPRODUCIBILITY

A. Training Hyperparameter

TABLE IV: Hyperparameters for PPO backend as used in AR-PO, RPL, and DRL.

Training Hyperparameter			
Total steps	2.5e <sup>6</sup>	Discount $\gamma$	0.99
Learning rate (LR)	1.5e <sup>-4</sup>	GAE $\lambda$	0.95
LR schedule	cos	Value coefficient	0.5
Trajectory length	1024	Max. gradient norm	0.5
Clip $\epsilon$	0.2	Update epochs	5
Batch size	512	Initial log $\sigma_{R,\theta}$	-1.0
Initial entropy	0.01	Final entropy	0.0
Entropy decay	linear		

B. Simulation Parameters

1) *Vehicle Model*: Parameters for the vehicle model in Table V are estimated from real-world Roboracer cars.

TABLE V: Simulation parameters for the single-track vehicle model.

Vehicle Parameter			
Vehicle mass in kg	3.3	Inertia in kg m <sup>2</sup>	0.0627
Vehicle width in m	0.27	Vehicle length in m	0.51
Distance front axle in m	0.1625	Distance rear axle in m	0.1625
CG height in m	0.02	Steering angle in rad	$\pm 0.45$
Max. velocity in m s <sup>-1</sup>	8.0	Min. velocity in m s <sup>-1</sup>	0.0
Max. acceleration in m s <sup>-2</sup>	4.9	Max. braking in m s <sup>-2</sup>	-3.7
Steering velocity in rad s <sup>-1</sup>	$\pm 3.2$	Lidar range in m	10.0
Lidar points	1081	Lidar FOV in $^\circ$	270
LiDAR frequency in Hz	40	Control frequency in Hz	40

2) *Tire Model*: Pacejka and Besselink [18]’s Magic Tire formula uses four coefficients for capturing nonlinear tire behavior. The parameter  $B$  controls the stiffness,  $C$  shapes the curve,  $D$  scales the peak force (normalized), and  $E$  governs the transition from linear to saturation behavior. The friction coefficient  $\mu$  scales the forces accordingly. Given the vehicle parameters and corresponding normal forces, a rendering of the lateral tire forces for the coefficients in Table VI is shown in Figure 6.

TABLE VI: Pacejka tire model parameters.

Parameter Values			
$\mu$	0.5	$B_r$	6.5
$B_f$	5.5	$C_r$	1.5
$C_f$	1.5	$D_r$	1.0
$D_f$	1.0	$E_r$	0.1
$E_f$	0.1		

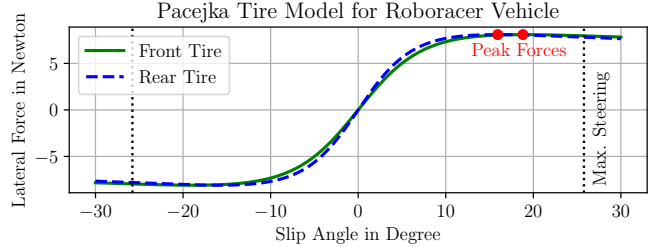


Fig. 6: Tire lateral forces over slip angle using Pacejka model.

C. Software

We list critical software with versions and used open-source repositories here:

- Python packages
  - Machine Learning: torch==2.9.0, torchrl==0.10.0
  - Others: NumPy==2.2.6, gymnasium==0.29.1
- Simulator: [https://github.com/raphajaner/TUM\\_FTRT\\_simulator](https://github.com/raphajaner/TUM_FTRT_simulator)
- Trajectory planning: [https://github.com/TUMFTM/global\\_racetrajectory\\_optimization](https://github.com/TUMFTM/global_racetrajectory_optimization)

## APPENDIX B RACETRACKS

Fig. 7: Visualization of the synthetically-generated racetracks used in this work. The shape is inspired by real-world Roboracer competition, including various challenging curvy and high-speed sections. Each racetrack's width varies between a plus-or-minus  $\pm 20\%$  of the mean width, which is randomly selected between 1.5 m and 1.8 m. The racetracks are named after famous cities from around the globe; however, there is no actual affiliation with the names. The last row shows the 5 racetracks only used for testing purposes and are not used for training.

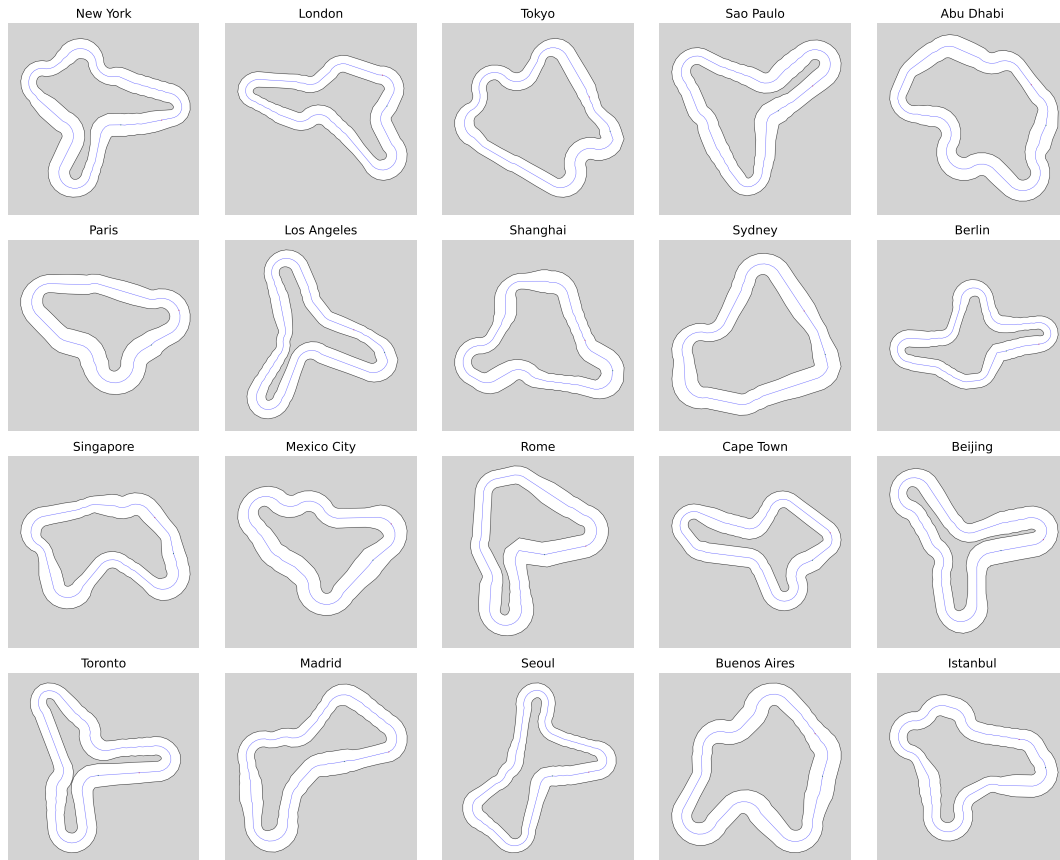


Fig. 8: Visualization of the *Munich* racetrack, based on a SLAM mapping of our real-world testbed.



APPENDIX C  
EXTENDED MATERIAL FOR EXPERIMENTS

A. Extended Race Results

TABLE VII: Results for simulated results, showing all 15 training and 6 testing maps. The *Munich* racetrack is an SLAM mapping of our real-world racetrack. A race finishes when 5 laps are completed. The best average results are highlighted in bold. The acronym BCD stands for BC+DRL, and DSSL is short for the DRL w/ SLL method. Note that due to numerical precision, average results can show zero collisions even when there are collisions on specific racetracks.

Racetrack	Total race time [s]					Collisions per lap [↓]					Max. speed [↑]										
	FTG	Stanley	DRL	BCD	DSSL	RPL	$\alpha$ -RPO	FTG	Stanley	DRL	BCD	DSSL	RPL	$\alpha$ -RPO	FTG	Stanley	DRL	BCD	DSSL	RPL	$\alpha$ -RPO
Abu Dhabi	67.54	50.41	48.50	46.29	49.55	48.16	44.02	0.00	0.00	0.03	0.00	0.01	0.09	0.00	4.32	5.06	4.81	4.72	4.83	5.15	5.15
Beijing	70.03	61.03	57.94	52.92	53.86	55.54	50.28	0.00	0.00	0.19	0.02	0.00	0.00	0.00	4.82	4.55	4.90	4.79	4.91	4.90	5.17
Berlin	75.32	63.49	58.59	57.10	57.83	60.17	54.81	0.00	0.00	0.00	0.00	0.00	0.00	0.00	4.43	4.97	5.08	4.92	4.87	5.01	5.28
Cape Town	72.64	57.25	51.88	51.19	52.39	51.95	49.15	0.00	0.00	0.00	0.00	0.00	0.00	0.00	4.98	4.69	5.01	4.88	4.93	4.94	5.28
London	71.04	55.72	55.73	50.05	51.25	52.57	47.58	0.00	0.00	0.20	0.00	0.00	0.04	0.00	5.03	4.81	5.00	4.84	4.96	5.10	5.29
Los Angeles	77.14	66.45	57.63	57.24	58.41	60.19	54.96	0.00	0.00	0.00	0.00	0.00	0.00	0.00	5.07	4.63	5.12	4.94	5.01	5.03	5.41
Mexico City	55.78	41.15	37.51	37.54	38.15	37.78	35.53	0.04	0.00	0.00	0.00	0.00	0.00	0.00	4.78	5.21	5.10	4.92	5.02	5.37	5.50
New York	71.88	63.08	54.49	54.00	55.09	56.17	51.95	0.00	0.00	0.00	0.00	0.00	0.00	0.00	4.58	4.45	5.08	4.95	5.02	4.89	5.34
Paris	51.40	39.74	41.08	35.88	36.68	35.78	34.13	0.00	0.00	0.19	0.00	0.00	0.00	0.00	4.48	5.32	5.25	5.00	5.03	5.41	5.50
Rome	73.55	52.90	48.20	48.09	48.98	48.99	45.61	0.12	0.00	0.00	0.00	0.00	0.00	0.00	5.16	5.37	5.23	4.96	5.05	5.42	5.59
Sao Paulo	71.34	57.90	53.01	51.82	52.71	55.63	49.80	0.00	0.00	0.00	0.00	0.00	0.00	0.00	4.44	5.35	5.20	5.07	5.00	5.23	5.53
Shanghai	64.94	48.34	46.88	46.46	46.60	46.63	44.89	0.00	0.00	0.01	0.00	0.00	0.00	0.00	4.32	5.08	5.19	5.00	5.07	5.30	5.55
Singapore	66.27	50.25	47.16	46.47	46.77	48.12	44.58	0.00	0.00	0.00	0.00	0.00	0.00	0.00	4.23	5.43	5.13	4.97	5.06	4.94	5.50
Sydney	55.95	44.52	40.18	40.16	40.90	40.43	38.37	0.00	0.00	0.00	0.00	0.00	0.00	0.00	4.94	4.98	5.23	4.91	4.98	5.38	5.44
Tokyo	71.32	55.53	49.98	49.46	50.93	49.53	47.96	0.06	0.00	0.00	0.00	0.00	0.00	0.00	4.87	5.14	5.25	5.02	5.06	5.51	5.58
Average Train	67.74	53.85	49.92	48.31	49.34	49.84	<b>46.24</b>	0.01	<b>0.00</b>	0.04	0.00	0.00	0.01	<b>0.00</b>	4.70	5.00	5.10	4.93	4.99	5.17	<b>5.41</b>
Buenos Aires	67.29	52.33	49.79	49.09	49.33	50.30	47.30	0.00	0.00	0.00	0.00	0.00	0.00	0.00	4.40	4.85	4.90	4.86	4.93	4.88	5.24
Istanbul	69.62	52.27	48.15	53.01	49.22	86.42	45.86	0.00	0.00	0.00	0.19	0.00	1.24	0.00	4.48	5.32	4.95	4.82	4.97	5.30	5.29
Madrid	66.91	53.51	49.66	49.09	49.60	50.87	47.28	0.00	0.00	0.00	0.00	0.00	0.00	0.00	4.97	4.46	5.03	4.88	4.89	4.79	5.32
Seoul	77.78	65.95	61.57	59.96	60.77	65.19	57.76	0.00	0.00	0.00	0.00	0.00	0.08	0.00	4.94	5.03	5.21	5.00	5.06	5.10	5.43
Toronto	76.31	65.20	59.63	57.92	58.64	62.67	55.58	0.00	0.00	0.00	0.00	0.00	0.00	0.00	5.18	4.60	5.16	4.95	5.04	4.95	5.35
<i>Munich</i>	38.10	32.77	41.87	33.60	30.15	32.71	28.91	0.00	0.00	0.41	0.14	0.00	0.01	0.00	3.41	4.29	4.69	4.70	4.70	4.46	4.92
Average Test	66.00	53.67	51.78	50.44	49.62	58.03	<b>47.11</b>	<b>0.00</b>	<b>0.00</b>	0.07	0.06	<b>0.00</b>	0.22	<b>0.00</b>	4.57	4.76	4.99	4.87	4.93	4.92	<b>5.26</b>

B. Further Trajectories

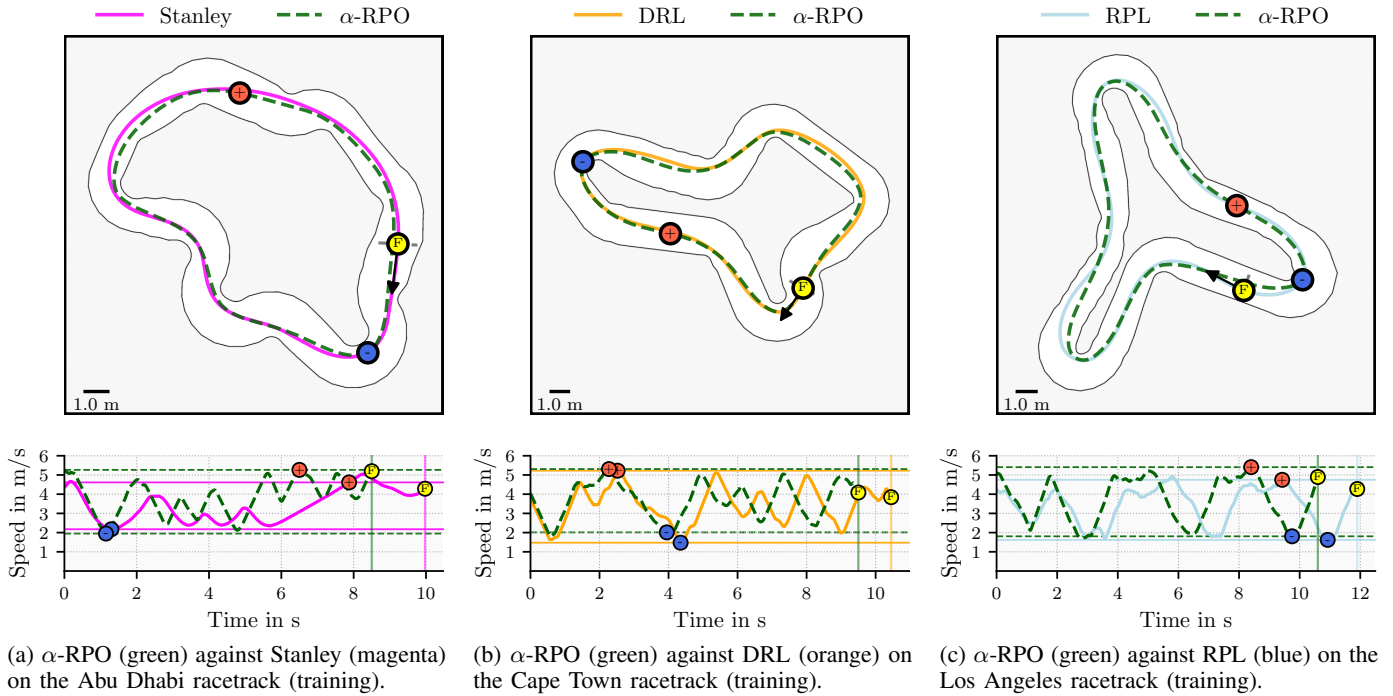


Fig. 9: Qualitative comparison of trajectories and speed profiles on three *training* racetracks of  $\alpha$ -RPO against Stanley (**left**), DRL (**mid**), and RPL (**right**). A single flying lap is shown, where markers indicate a specific POI on the racetracks: + marks a high-speed section (red), - indicates the section with minimal speed (blue), while F is the finish line (yellow).

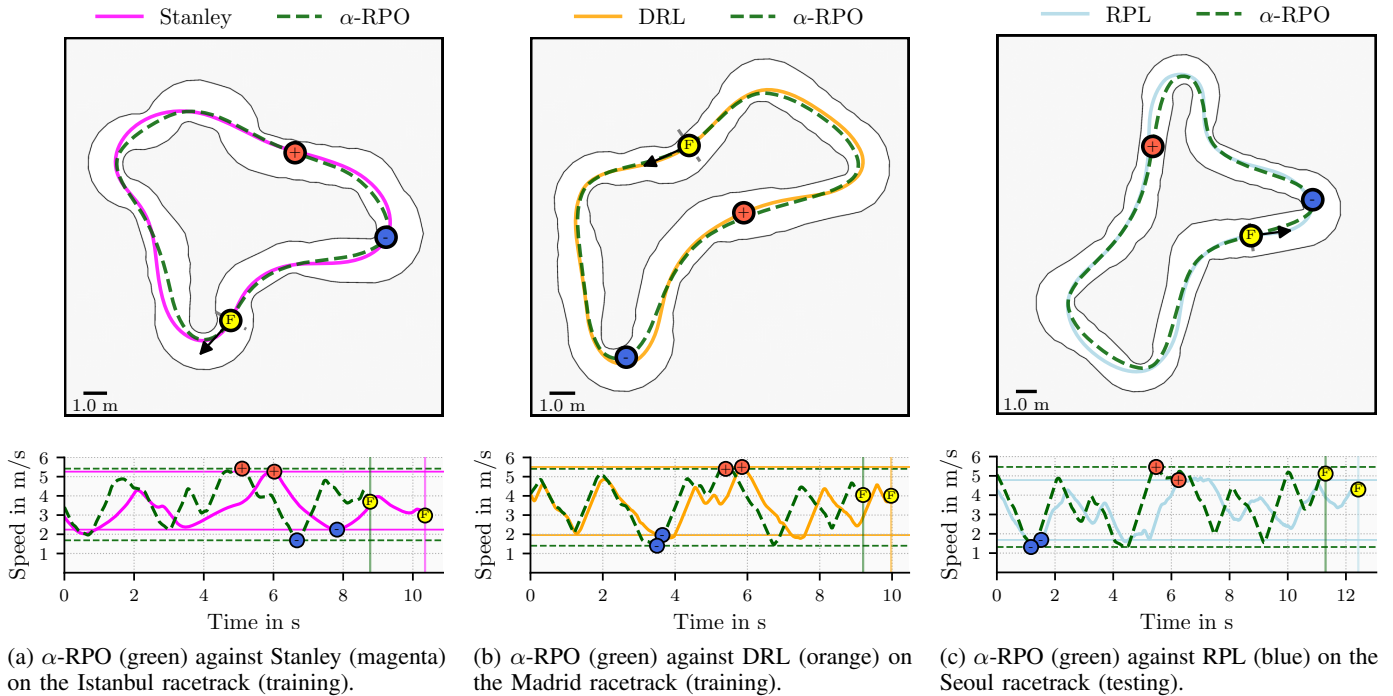


Fig. 10: Qualitative comparison of trajectories and speed profiles on three *testing* racetracks of  $\alpha$ -RPO against Stanley (**left**), DRL (**mid**), and RPL (**right**). A single flying lap is shown, where markers indicate a specific POI on the racetracks: + marks a high-speed section (red), - indicates the section with minimal speed (blue), while F is the finish line (yellow).

### C. Further Real-World Trajectories

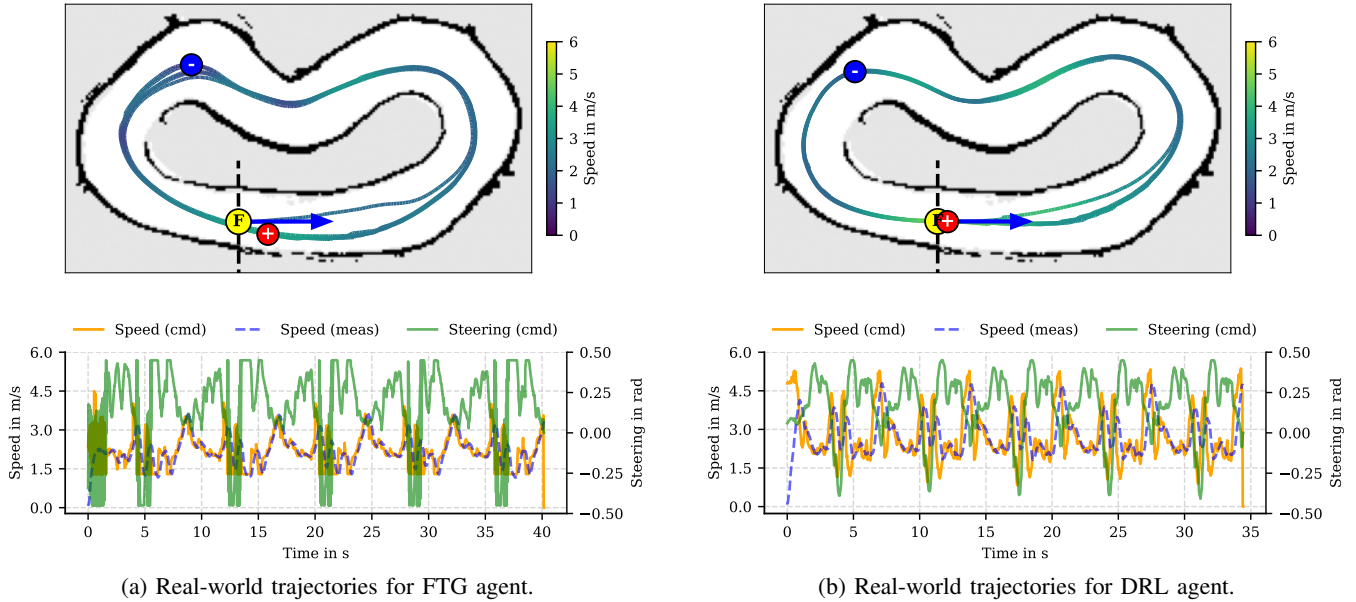


Fig. 11: Real-world trajectories for FTG (**left**) and DRL (**right**) agents on the *Munich* racetrack for 5 laps; current speed shown as color bar. Positions are estimated offline from `rosvbag` data using SLAM. The agent’s actions command (cmd) and measured speed (meas.) are also shown. Markers indicate a specific POI on the racetracks: + marks a high-speed section (red), – indicates the section with minimal speed (blue), while F is the finish line (yellow).

### D. Finetuning Comparison

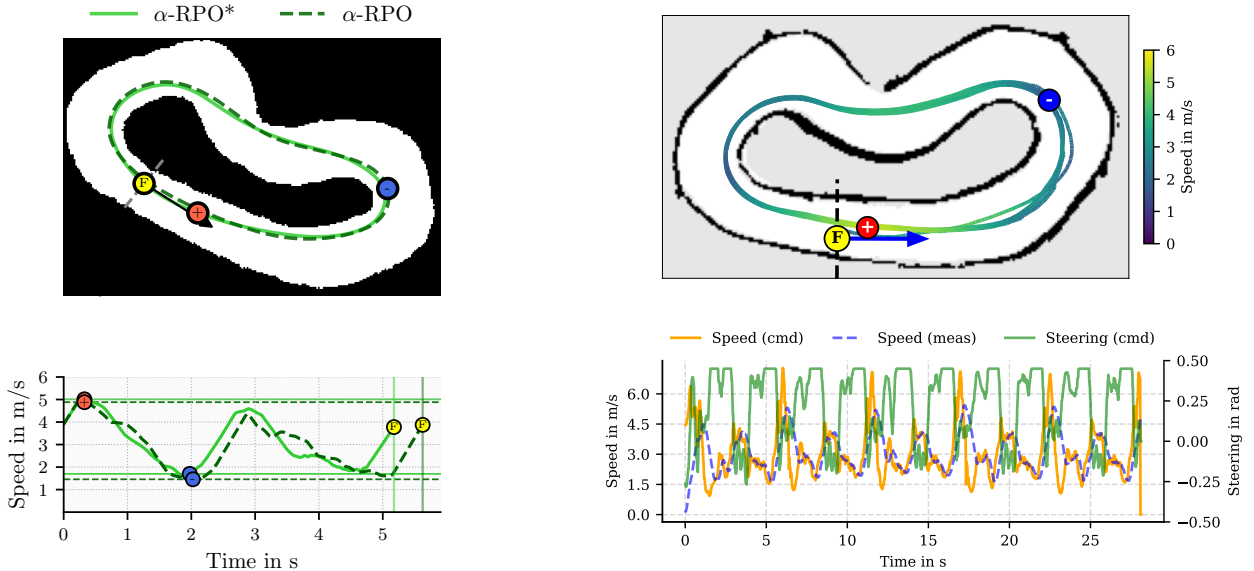


Fig. 12: Trajectories on the *Munich* racetrack for 5 laps, comparing the  $\alpha$ -RPO agent to the finetuned  $\alpha$ -RPO\* version in simulation (**left**) and showing its real-world behavior (**right**). It can be seen that  $\alpha$ -RPO\* shows superior performance, particularly in the left-right section at the top, by cutting it straight with higher speed. The real-world trajectory shows the current speed as a color bar; positions are estimated offline from `rosvbag` data using SLAM. The agent’s actions command (cmd) and measured speed (meas.) are also shown. Markers indicate a specific POI on the racetracks: + marks a high-speed section (red), – indicates the section with minimal speed (blue), while F is the finish line (yellow).

### A. Architecture

In this work, we employ a DNN architecture based on a shared encoder structure but with separate heads for the residual network  $f_\theta$  and critic network  $f_\phi$ , totaling 344,357 trainable parameters; see Table VIII for parameter counts per layer.

The architecture processes the downsampled LiDAR scan  $L'_t \in [0, 1]^{512}$  and the normalized vehicle state  $s'_t$ , which is a subset of  $s_t$  excluding  $L_t$ , separately, and then fuses their embeddings. The *LidarEncoder* processes  $L'_t$  via a stack of five Conv1d layers, each with a kernel size of 3 and a stride of 2. To extract a compact feature representation from the resulting feature maps, we apply an AdaptiveSpatialSoftmax1d layer with  $K = 4$  keypoints; see Section D-B. The resulting reduced feature vector is followed by a Linear projection, yielding the final LiDAR embedding  $z_t \in \mathbb{R}^{128}$ . Parallel to this, the vehicle state is encoded by the *StateEncoder*, consisting of two stacked Linear layers, to produce the state embedding  $h_t \in \mathbb{R}^{128}$ . These embeddings,  $z_t$  and  $h_t$ , are concatenated and refined within the *FusionBlock* via LayerNorm normalization followed by a Linear layer to fuse them to the final embedding  $z'_t$ . This fused feature vector serves as the input to three independent fully-connected heads that build the residual network  $f_\theta$  and critic network  $f_\phi$ . The *PolicyHead* and the *LogStdHead* feature both a hidden dimension of 256, while the *CriticHead* has a higher hidden dimension of 512 for increased descriptive capacity.

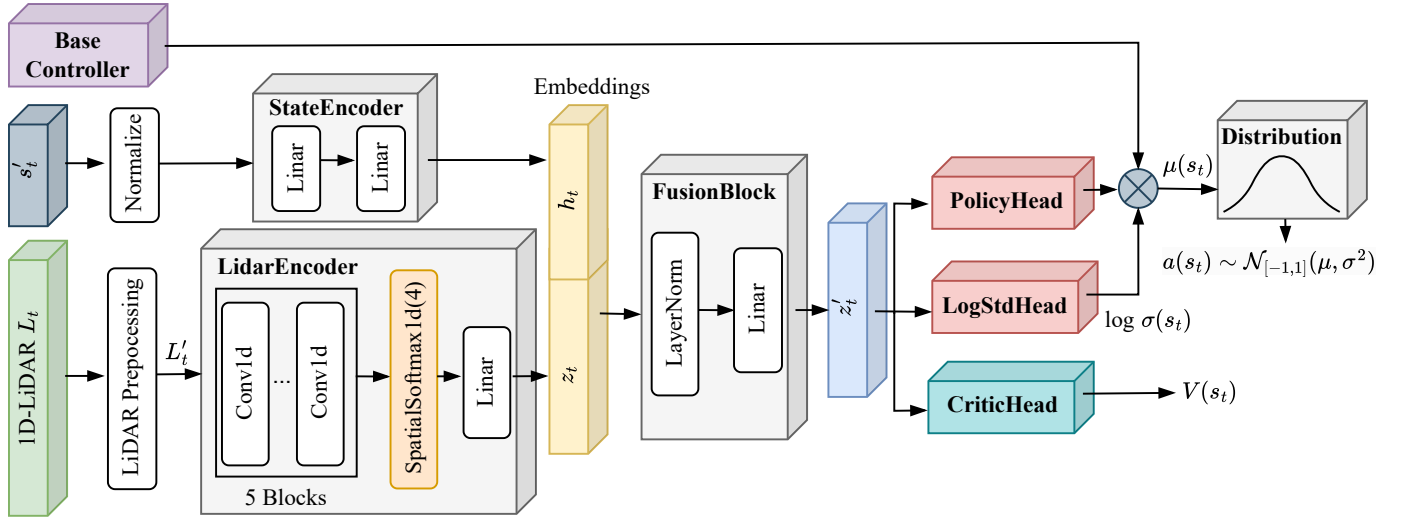


Fig. 13: Proposed DNN architecture. The input to the *LidarEncoder* is the stacked, processed LiDAR observations  $L'_t$ , and the *StateEncoder* input is the normalized vehicle state  $s'_t$ , which is the subset of  $s_t$  without  $L_t$ . The *FusionBlock* outputs the embeddings  $z'_t$ , which are fed into the three independent heads: *PolicyHead*, *LogStdHead*, and *CriticHead*.

### B. Adaptive SpatialSoftmax1d Layer

To efficiently transition from high-dimensional 1D sensor features to a compact state representation, we employ an adaptive *SpatialSoftmax1d* layer. This mechanism adapts the deep spatial autoencoder architecture [8] to 1D sequence data, serving as a learnable, geometry-preserving alternative to adaptive AveragePooling, which has recently shown great promise to improve generalization in visual DRL [27]. Unlike standard pooling, which degrades or even removes spatial information, or flattening, which results in a large feature vector, this layer reduces the feature space while retaining topological structure.

The adaptive *SpatialSoftmax(K)* layer compresses a feature map  $X \in \mathbb{R}^{C \times L}$  of arbitrary length  $L$  into a compact, fixed set of  $K$  spatial keypoints for each of the  $C$  channels. The input sequence is first partitioned into  $K$  equal-length segments. For each channel  $c$  and segment  $k$ , we compute a local probability distribution  $P_{c,k}$  over the segment's domain by applying a softmax function

$$P_{c,k}(i) = \frac{\exp(X_{c,k,i}/T)}{\sum_j \exp(X_{c,k,j}/T)}, \quad (11)$$

where the temperature is typically set to  $T = 1$ . We then compute the expected 1D position  $\hat{x}_{c,k}$  within the segment's local coordinate frame

$$\hat{x}_{c,k} = \sum_i \xi_i \cdot P_{c,k}(i) \quad (12)$$

where  $\xi \in \mathbb{R}^{L/K}$  is a fixed linear coordinate grid linearly spaced in the interval  $[-1, 1]$ , representing the normalized position within any given segment. The computed scalar keypoints  $\hat{x}_{c,k}$  for all channels  $c \in \{1, \dots, C\}$  and segments  $k \in \{1, \dots, K\}$

are concatenated to form the final output tensor  $\hat{X} \in \mathbb{R}^{C \times K}$ . As such, the SpatialSoftmax(K) layer leads to a reduction of the feature space by a factor of  $L/K$ .

### C. Parameter Counts

TABLE VIII: Summary with parameters counts per layer of the DNN model.

Layer Type	Parameter Count	%	Kernel	Input Size	Output Size
└ <b>Encoder</b>	–	–	–	[B, 4, 1081]	[B, 128]
└└ LidarPreprocessor	–	–	–	[B, 4, 1081]	[B, 4, 512]
└└└ AvgPool1d	–	–	[2]	[B, 4, 1024]	[B, 4, 512]
└└ LidarEncoder	–	–	–	[B, 4, 512]	[B, 128]
└└└ Conv1d	416	0.12%	[3]	[B, 4, 512]	[B, 32, 256]
└└└ SiLU	–	–	–	[B, 32, 256]	[B, 32, 256]
└└└ Conv1d	6,208	1.80%	[3]	[B, 32, 256]	[B, 64, 128]
└└└ SiLU	–	–	–	[B, 64, 128]	[B, 64, 128]
└└└ Conv1d	12,352	3.59%	[3]	[B, 64, 128]	[B, 64, 64]
└└└ SiLU	–	–	–	[B, 64, 64]	[B, 64, 64]
└└└ Conv1d	24,704	7.17%	[3]	[B, 64, 64]	[B, 128, 32]
└└└ SiLU	–	–	–	[B, 128, 32]	[B, 128, 32]
└└└ Conv1d	49,280	14.31%	[3]	[B, 128, 32]	[B, 128, 16]
└└└ AdaptSpatSoftmax1D	–	–	–	[B, 128, 16]	[B, 128, 4]
└└└ Flatten	–	–	–	[B, 128, 4]	[B, 512]
└└└ Linear	65,664	19.07%	–	[B, 512]	[B, 128]
└└ StateEncoder	–	–	–	[B, 16]	[B, 128]
└└└ Linear	2,176	0.63%	–	[B, 16]	[B, 128]
└└└ SiLU	–	–	–	[B, 128]	[B, 128]
└└└ Linear	16,512	4.80%	–	[B, 128]	[B, 128]
└└ FusionBlock	–	–	–	[B, 128]	[B, 128]
└└└ LayerNorm	512	0.15%	–	[B, 256]	[B, 256]
└└└ Linear	32,896	9.55%	–	[B, 256]	[B, 128]
└ <b>CriticHead</b>	–	–	–	[B, 128]	[B, 1]
└└ Linear	66,048	19.18%	–	[B, 128]	[B, 512]
└└ SiLU	–	–	–	[B, 512]	[B, 512]
└└ Linear	513	0.15%	–	[B, 512]	[B, 1]
└ <b>PolicyHead</b>	–	–	–	[B, 128]	[B, 2]
└└ Linear	33,024	9.59%	–	[B, 128]	[B, 256]
└└ SiLU	–	–	–	[B, 256]	[B, 256]
└└ Linear	514	0.15%	–	[B, 256]	[B, 2]
└ <b>LogStdHead</b>	–	–	–	[B, 128]	[B, 2]
└└ Linear	33,024	9.59%	–	[B, 128]	[B, 256]
└└ SiLU	–	–	–	[B, 256]	[B, 256]
└└ Linear	514	0.15%	–	[B, 256]	[B, 2]
<b>Total parameters:</b>	<b>344,357</b>				